

Effects of Ion-Induced Displacement Damage on GaN/AlN MEMS Resonators

Wen Sui¹, *Student Member, IEEE*, Xu-Qian Zheng², *Member, IEEE*, Ji-Tzuoh Lin³,

Jaesung Lee⁴, *Member, IEEE*, Jim L. Davidson⁵, *Senior Member, IEEE*,

Robert A. Reed⁶, *Fellow, IEEE*, Ronald D. Schrimpf⁷, *Fellow, IEEE*, Bruce W. Alphenaar⁸, *Member, IEEE*,

Michael L. Alles, *Senior Member, IEEE*, and Philip X.-L. Feng⁹, *Senior Member, IEEE*

Abstract—Gallium nitride (GaN) has attracted great attention as a structural material for advanced microelectromechanical systems (MEMS), thanks to its excellent ensemble of electrical and mechanical properties. Here, we report on studying the effects of ion radiation-induced displacement damage on resonant MEMS made of GaN film grown on aluminum nitride (AlN) buffer layer. We design and fabricate GaN/AlN heterostructure doubly-clamped microstring resonators with length $L = 100, 200, 300, 400, 500, 600,$ and $700 \mu\text{m}$, and irradiate the devices with 440-keV Ar^+ ions, to probe the effects of ion radiation-induced displacement damage on the resonance behavior. The ion energy and range have been selected so that the ions would stop within the GaN layer, thus allowing diagnostics to show the effects of damage in the structure. The multimode resonance frequencies of the devices decrease significantly ($|\Delta f|/f > 50\%$) with the increase of fluence beyond 10^{14} cm^{-2} . According to scanning electron microscopy (SEM) imaging, the irradiated GaN/AlN resonators are visibly deformed at high fluence, where the amount of curvature increases monotonically with the fluence. The deformation of the structures can be ascribed to the change in both Young's modulus and built-in stress resulting from ion radiation-induced displacement damage. The results extend the understanding of radiation-induced damage mechanisms in resonant MEMS.

Index Terms—Displacement damage, gallium nitride (GaN), GaN/aluminum nitride (AlN) heterostructure, multimode, radiation, resonator, stress.

Manuscript received November 3, 2021; revised December 23, 2021; accepted December 26, 2021. Date of publication January 14, 2022; date of current version March 16, 2022. This work was supported by the Defense Threat Reduction Agency (DTRA) through the Basic Scientific Research Program under Grant HDTRA1-19-1-0035 and Grant HDTRA1-15-1-0027. (Wen Sui and Xu-Qian Zheng contributed equally to this work.)

Wen Sui, Xu-Qian Zheng, Jaesung Lee, and Philip X.-L. Feng are with the Department of Electrical and Computer Engineering, Herbert Wertheim College of Engineering, University of Florida, Gainesville, FL 32611 USA (e-mail: wen.sui@ufl.edu; xuqian.zheng@ufl.edu; jaesung.lee@ufl.edu; philip.feng@ufl.edu).

Ji-Tzuoh Lin and Bruce W. Alphenaar are with the Department of Electrical and Computer Engineering, University of Louisville, Louisville, KY 40292 USA (e-mail: jitzuoh.lin@louisville.edu; bruce.alphenaar@louisville.edu).

Jim L. Davidson, Robert A. Reed, Ronald D. Schrimpf, and Michael L. Alles are with the Department of Electrical Engineering and Computer Science, Vanderbilt University, Nashville, TN 37235 USA (e-mail: jim.davidson@vanderbilt.edu; robert.reed@vanderbilt.edu; ron.schrimpf@vanderbilt.edu; mike.alles@vanderbilt.edu).

Color versions of one or more figures in this article are available at <https://doi.org/10.1109/TNS.2022.3143550>.

Digital Object Identifier 10.1109/TNS.2022.3143550

I. INTRODUCTION

ADVANCES in materials science and fabrication techniques offer new opportunities for microelectromechanical systems (MEMS), including gyroscopes, accelerometers, radio frequency (RF) resonators, oscillators, and switches, as well as biosensors and micromirrors [1]–[5]. The significantly reduced size, weight, and power (SWaP) of MEMS are attractive for a wide spectrum of applications ranging from consumer and medical areas to military and space missions [6]–[8]. In addition to the improving performance, long-term stability is also important for MEMS employed in radiation environments, such as devices for space missions [9], [10]. It is thus necessary and important to investigate the effects of radiation on MEMS for both temporary influence and long-term reliability [11], [12]. Both ionizing radiation and nonionizing radiation play key roles in affecting the performance of MEMS [13]. Dielectric charging from ionizing radiation can affect the mechanical structure and alter the resonant frequency by electrostatic force [14]. Displacement damage originating from nonionizing energy loss (NIEL) can introduce permanent damage to materials and change mechanical properties [15]. The degradation of MEMS caused by radiation differs depending on their designs and operating principles. Radiation induced dielectric charging may potentially limit the reliability of electrostatically actuated MEMS, while thermally actuated MEMS and piezoelectric MEMS are much more tolerant to ionizing radiation. Optical drive and interferometry-based detection are decoupled from charging, thus capable of retaining and probing the effects of dielectric charging on resonant MEMS [16]. Diverse sensing schemes and a wide range of materials make it challenging to predict the device behaviors and to improve the reliability of MEMS under radiation.

To date, studies of radiation effects on MEMS are still limited and largely focused on silicon (Si) devices. Young's modulus and the yield strength of many Si devices do not change a lot at typical particle fluences encountered in space, but MEMS such as resonators may be sensitive to parts-per-million levels of variations in stiffness, which depends on the Young's modulus and built-in stress of the device. Although Si still dominates the mainstream MEMS industry, a number of wide bandgap (WBG) semiconductors, including gallium

nitride (GaN), aluminum nitride (AlN), and silicon carbide (SiC), have attracted growing attention for MEMS applications, especially for high-voltage, high-power scenarios, and in harsh environments. Among them, GaN is an important WBG material ($E_{g,\text{GaN}} = 3.4$ eV) with outstanding electrical properties for high-power and high-frequency electronics; it also has excellent Young's modulus ($E_{Y,\text{GaN}} = 250\text{--}400$ GPa) and intrinsic piezoelectricity. This strong ensemble of compelling properties makes GaN attractive as a structural material for MEMS [17]. While displacement damage in Si [18], [19] and SiC [20] MEMS has been investigated, previous radiation studies on GaN MEMS have mainly been limited to photon radiation effects [21], [22].

In this work, we design and fabricate GaN/AlN heterostructure (GaN grown on AlN buffer) MEMS resonators, in microstring geometry, with length $L = 100, 200, 300, 400, 500, 600,$ and 700 μm . We irradiate the devices with 440-keV argon ions (Ar^+) to fluences (Φ) ranging from 5×10^{11} to 1×10^{15} cm^{-2} . We employ a customized optical laser interferometry system to investigate the changes of mechanical properties induced by displacement damage to the GaN/AlN MEMS resonators. Raman and scanning electron microscopy (SEM) are utilized to investigate the changes of morphology and crystallinity induced by displacement damage.

II. DESIGN OF THE EXPERIMENT

We irradiate the MEMS devices with normal-incidence Ar^+ ions with energy of 440 keV. The crystallinity and stress changes in the GaN thin film are examined via Raman spectroscopy. GaN/AlN doubly-clamped microstring resonators with different length are used to investigate the radiation effects on mechanical properties. By measuring the resonance frequencies of the GaN/AlN resonators before and after radiation, the built-in stress and Young's modulus are extracted and compared, which allow us to gain understanding of the mechanical properties of the devices upon irradiation. Finally, SEM is utilized to characterize the morphology of the GaN/AlN resonators before and after the ion irradiation.

A. Design of Radiation Exposure

To ensure that major displacement damage events occur in the GaN/AlN device layer, the energy and ion species are selected so that the ions stop within the 700-nm-thick GaN/AlN heterostructure [Fig. 1(a)]. Simulations by the stopping and range of ions in matter (SRIM) software show that all the 440-keV Ar^+ stop in the GaN layer [Fig. 1(b) and (c)] and the displacement damage (creation of vacancies) is confined to the GaN film [Fig. 1(d)]. The absorbed dose due to nonionizing effects is estimated by considering the number of vacancies produced for both the incident particle and resultant recoils. The vacancy formation rate is then converted to NIEL using the Kinchin–Pease relationship [23]. Fig. 1(e) shows the NIEL result for Ar^+ with energy of 440 keV as a function of the penetration depth. We irradiate our MEMS devices with 440-keV Ar^+ to fluences ranging from 5×10^{11} to 10^{15} cm^{-2} . The displacement damage doses obtained from the product of the particle fluence and the NIEL are on the order of

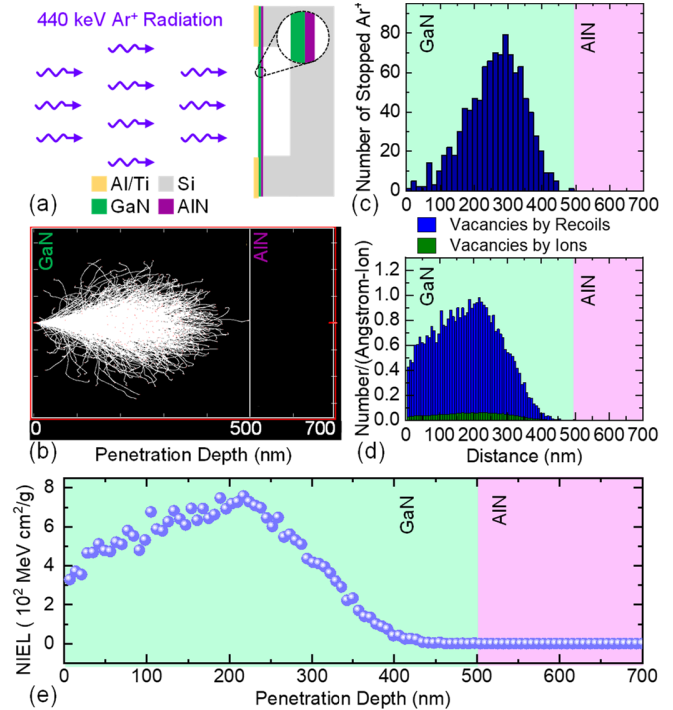


Fig. 1. (a) 440-keV Ar^+ radiation on GaN/AlN devices. (b) SRIM simulation of 1000 Ar^+ ions on GaN/AlN structure. (c) Distribution of stopped Ar^+ ions. (d) Distribution of displacement damage induced vacancies. (e) NIEL as a function of penetration depth for Ar^+ in GaN computed using SRIM.

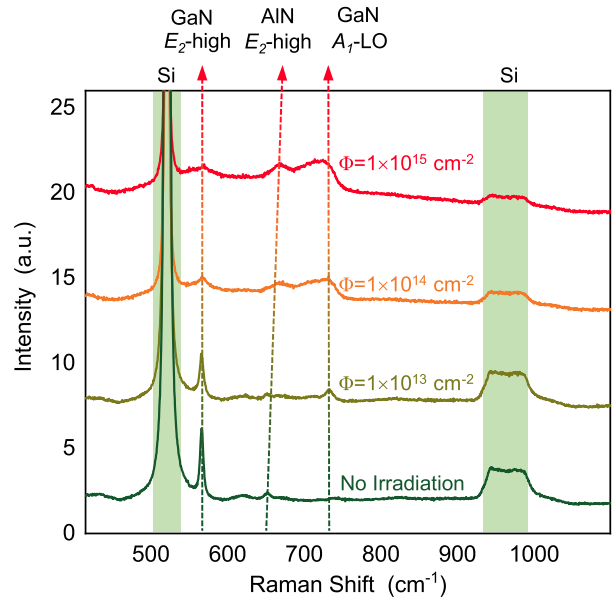


Fig. 2. Raman spectra of supported GaN/AlN heterostructure on Si (111) substrate with and without irradiation.

$10^{13}\text{--}10^{17}$ MeV/g. The fluence levels we use are very high relative to what would be encountered in the natural space environment; but these levels are useful for understanding potential degradation mechanisms and ensuring that there are no unexpected results at lower damage levels.

B. Raman Shift After Radiation

To understand the effects of radiation on the crystallinity of GaN and the built-in stress in the GaN layer, Fig. 2 shows the

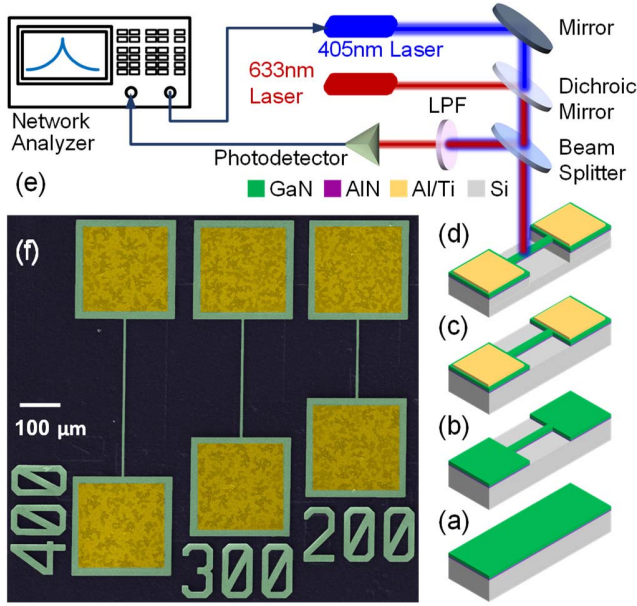


Fig. 3. Device fabrication and optical interferometry measurement system. (a) GaN/AlN on Si substrate. (b) Dry etching of GaN/AlN. (c) Contact pad deposition. (d) XeF₂ etching of Si to release the GaN/AlN resonator. (e) Ultrasensitive laser interferometry system for driving and detecting the resonance motion of the GaN/AlN doubly-clamped resonators. (f) Colored SEM image showing the typical devices with $L = 200, 300, \text{ and } 400 \mu\text{m}$.

Raman spectra of the GaN/AlN heterostructure on Si (111) substrate for both unirradiated and irradiated samples with fluences of 10^{13} cm^{-2} , 10^{14} cm^{-2} , or 10^{15} cm^{-2} . Consistent with literature reports, both the E_2 -high and A_1 -local oscillator (LO) modes of GaN are observed at 566.4 and 733.3 cm^{-1} , respectively, for the unirradiated sample [24]. The shift of the E_2 -high phonon mode is utilized to quantify the stress/strain present in the grown film. For stress-free GaN film, the E_2 -high mode should be located at 567.6 cm^{-1} . The blue shift of the E_2 -high mode indicates that the stress in the GaN layer is tensile. The E_2 -high mode peak of GaN gradually broadens with increasing fluence from 0 to 10^{15} cm^{-2} , implying gradual deterioration of the crystallinity of the GaN. At high fluences ($\Phi \geq 10^{14} \text{ cm}^{-2}$), the E_2 -high mode peak of GaN decreases significantly. As we shall discuss later, this decrease in crystallinity is responsible for the deteriorated mechanical properties of the devices irradiated with high fluences ($\Phi \geq 10^{14} \text{ cm}^{-2}$). Moreover, we assign the peak at 651.3 cm^{-1} to be the E_2 -high mode of the AlN. It is also seen that its position is radiation dependent, suggesting different stress states within the layers.

C. GaN/AlN Doubly-Clamped Resonators

A doubly-clamped resonator structure is chosen and the built-in stress and Young's modulus can be extracted from the resonance frequency. Fig. 3(a)–(d) shows the fabrication process of the devices. The GaN/AlN wafer from Kyma Technologies consists of a thin layer of crystalline GaN (500 nm) grown by hydride vapor phase epitaxy (HVPE) and an intermediate nucleation layer of crystalline AlN (200 nm) on a Si substrate. The fabrication starts with photolithography

and the deposition of chromium (Cr) as a hard mask, followed by dry etching of the GaN and AlN. After removing the Cr mask, another photolithography step is conducted to pattern the Al on titanium (Ti) contact pads. Finally, the GaN/AlN doubly-clamped resonators are released by etching of Si in xenon difluoride (XeF₂).

D. Optical Interferometry Measurement

The resonances of the devices are characterized by an ultrasensitive laser interferometry system [25], as shown in Fig. 3(e), which consists of: 1) 405-nm amplitude-modulated laser to photothermally excite resonances; 2) 633-nm laser focused on the device to detect the device motion interferometrically; 3) photodetector to transduce the time-varying optical interferometric signals into electrical signals; and 4) network analyzer to drive and read out the frequency response. Such measurement provides an accurate measure of the mechanical resonance frequency [26]. The laser induced shift in resonance frequency due to the parasitic heating from the photothermal effect is negligible compared with the stress induced change in resonance frequency under different radiation fluences.

E. Scanning Electron Microscopy

SEM is used to characterize the morphology of the GaN/AlN resonators before and after the ion irradiation, in which the curvature (profile) of the device can be acquired. It provides an intuitive way to understand how the radiation affects the morphology of the devices. Fig. 3(f) shows a colored SEM image of typical devices before radiation.

III. RESULTS AND DISCUSSIONS

A. Radiation Effects on the Resonance of Fundamental Mode

The resonance frequency of the out-of-plane fundamental flexural mode of the GaN/AlN doubly-clamped resonator can be expressed as [27]

$$f_1 = \frac{9\pi}{8L^2} \sqrt{\frac{E_Y I}{\rho \omega t}} \sqrt{1 + \frac{0.243\sigma \omega t L^2}{\pi^2 E_Y I}} \quad (1)$$

where $I = \omega t^3/12$ is the moment of inertia; L , ω , and t are length, width, and thickness of the doubly-clamped device, respectively, with $\omega = 5 \mu\text{m}$ and $t = t_{\text{GaN}} + t_{\text{AlN}} = 500 \text{ nm} + 200 \text{ nm} = 700 \text{ nm}$. Here, $E_Y = (E_{Y,\text{GaN}} t_{\text{GaN}} + E_{Y,\text{AlN}} t_{\text{AlN}})/(t_{\text{GaN}} + t_{\text{AlN}})$ and $\rho = (\rho_{\text{GaN}} t_{\text{GaN}} + \rho_{\text{AlN}} t_{\text{AlN}})/(t_{\text{GaN}} + t_{\text{AlN}})$ are the effective Young's modulus and the effective mass density of the GaN/AlN heterostructure, respectively, and σ is the built-in stress in the suspended structure. We first measure and model the fundamental mode resonance of the unirradiated GaN/AlN doubly-clamped resonators on a chip (Chip 1), with $L = 100, 130, 200, 300, 400, 500, 600, \text{ and } 700 \mu\text{m}$. The fundamental mode resonance frequencies are centered at 1.853, 1.338, 0.863, 0.564, 0.416, 0.328, 0.272, and 0.257 MHz, respectively [Fig. 4(a)]. The measured resonance frequencies agree well with the analytical model [see (1)] by using $E_{Y,\text{GaN}} = 360 \text{ GPa}$, $E_{Y,\text{AlN}} = 344 \text{ GPa}$, $\rho_{\text{GaN}} = 6150 \text{ kg/m}^3$, $\rho_{\text{AlN}} = 3260 \text{ kg/m}^3$, and $\sigma = 600 \text{ MPa}$. We then directly compare the fundamental

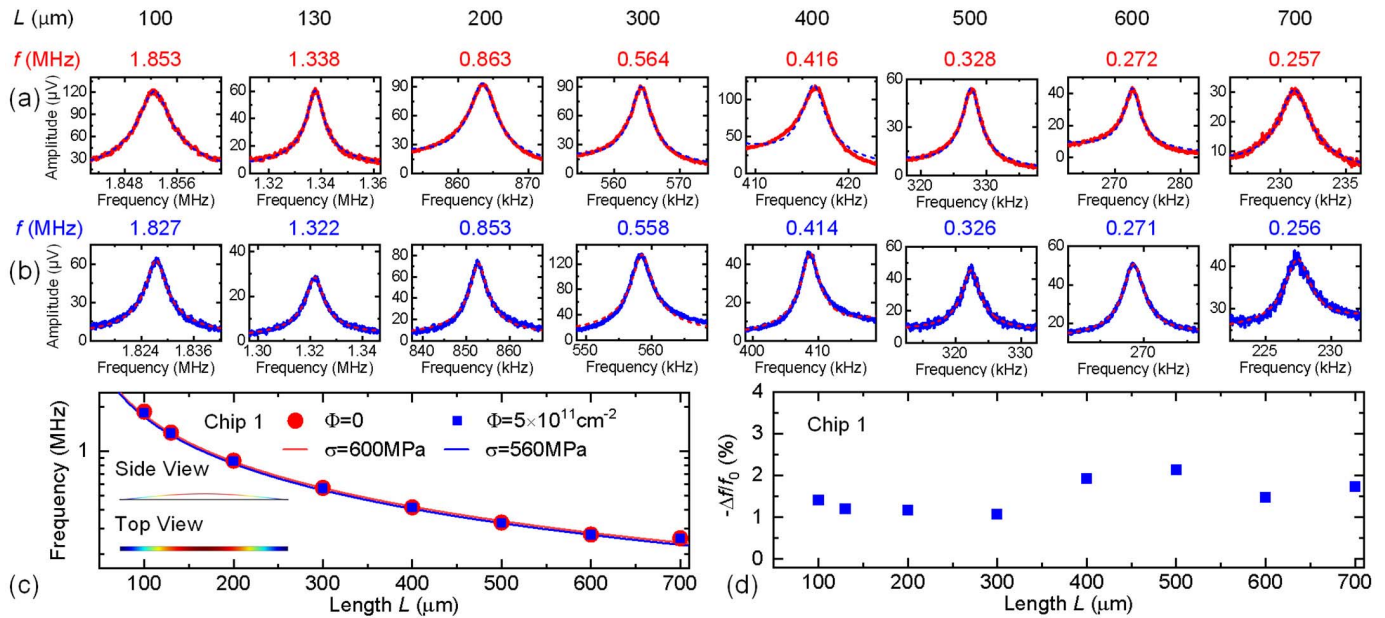


Fig. 4. Fundamental mode resonance spectra of devices with $L = 100, 130, 200, 300, 400, 500, 600,$ and $700 \mu\text{m}$ (a) before and (b) after radiation with $\Phi = 5 \times 10^{11} \text{cm}^{-2}$. (c) Resonance frequency fitting with elastic resonator model [see (1)]. (d) Fractional downshift of resonance frequency.

mode resonance frequencies of the GaN/AlN doubly-clamped resonators on Chip 1 before and after radiation with the fluence of $5 \times 10^{11} \text{cm}^{-2}$. The resonance spectra of different devices after radiation and the fractional downshift of resonance frequencies are shown in Fig. 4(b)–(d). We find the fractional downshift of the resonance frequencies for devices with different lengths is quite consistent, *i.e.*, all within the range of 1%–2.5%. One possible contributor to the downshift of the resonance frequency is the effect of mass loading caused by stopped ions in the GaN layer. However, only <10 ppm of added areal mass density is introduced by $5 \times 10^{11} \text{cm}^{-2} \text{Ar}^+$ irradiation. Such small added areal mass density is negligible compared with the much more significant change in resonance frequency observed in measurement. Consequently, the changes in the resonance characteristics can be attributed to variations of built-in stress and Young’s modulus.

To understand how built-in stress and Young’s modulus affect the resonance frequency, we conduct analysis of frequency scaling upon E_Y and σ variations for GaN/AlN doubly-clamped resonators with $L = 200 \mu\text{m}$, $L = 400 \mu\text{m}$, and $L = 600 \mu\text{m}$, respectively (Fig. 5). Within the whole range of E_Y from 50 to 550 GPa, the resonance frequencies of the fundamental out-of-plane flexural mode are nearly independent of E_Y , with the frequencies maintained at 0.863, 0.416, and 0.272 MHz, respectively [Fig. 5(a)]. Given the large length-to-thickness aspect ratio (L/t), σ rather than E_Y plays a dominant role in determining the resonance frequency for this mode. With large σ , we can use the stress-dominant “string” model to describe the n th out-of-plane (V_n) mode’s resonance frequency

$$f_{Vn} = \frac{n}{2L} \sqrt{\frac{\sigma}{\rho}}. \quad (2)$$

As shown in Fig. 5(b), the resonance frequency gradually increases with the increase of built-in stress. We can conclude

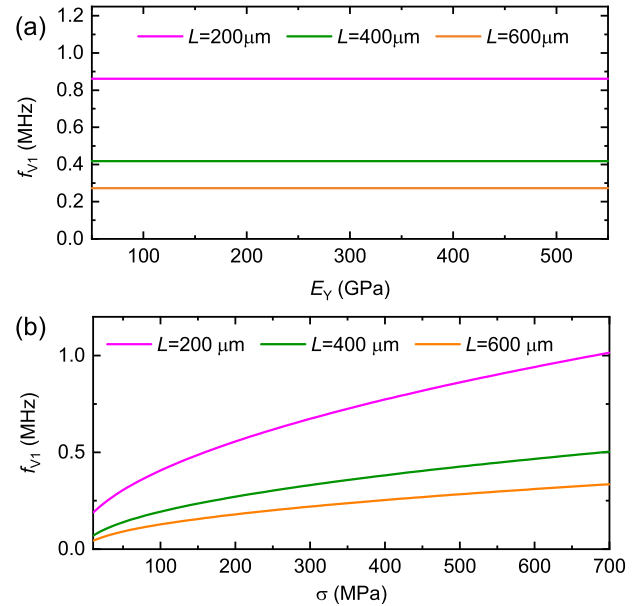


Fig. 5. Frequency scaling (f) upon (a) E_Y and (b) σ variation of the fundamental out-of-plane flexural mode (V_1) for GaN/AlN doubly-clamped resonators with $L = 200 \mu\text{m}$, $L = 400 \mu\text{m}$, and $L = 600 \mu\text{m}$, respectively.

that the resonance frequency of the out-of-plane fundamental mode is determined by the stress σ inside the GaN/AlN layer. As shown in Fig. 4(c), the measured resonance frequencies after radiation to a fluence of $5 \times 10^{11} \text{cm}^{-2}$ agree well with the analytical model [see (2)] by using $\sigma = 560 \text{MPa}$. Note that the effect of variation of Young’s modulus is not considered due to its negligible effect. Thus, 40-MPa decrease of built-in stress is induced after radiation with fluence of $5 \times 10^{11} \text{cm}^{-2}$.

We then irradiate the GaN/AlN doubly-clamped resonators on another chip (Chip 2), with $L = 130, 200, 300,$ and

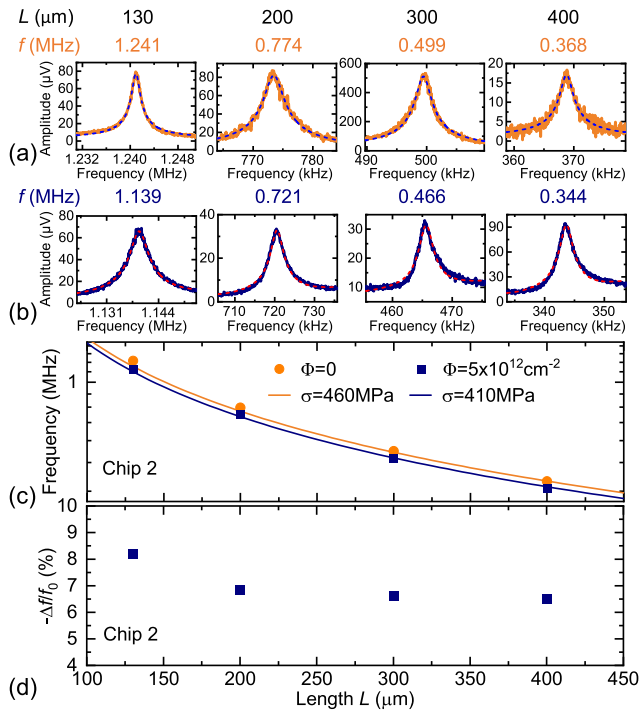


Fig. 6. Fundamental mode resonance spectra of devices with $L = 130, 200, 300,$ and $400 \mu\text{m}$. (a) Before and (b) after radiation with fluence of $\Phi = 5 \times 10^{12} \text{ cm}^{-2}$. (c) Resonance frequency fitting with elastic resonator model [see (1)]. (d) Measured fractional downshift of resonance frequency versus device length.

$400 \mu\text{m}$, by 400-keV Ar^+ with the fluence of $5 \times 10^{12} \text{ cm}^{-2}$. According to the measured resonance spectra before and after radiation [Fig. 6], Ar^+ irradiation with a fluence of $5 \times 10^{12} \text{ cm}^{-2}$ induces a significant decrease in resonance frequency, with the fractional downshift magnitude in the range of 6%–8% [Fig. 6(c) and (d)]. Both the resonance frequencies measured before and after radiation agree well with the analytical model [see (2)]. The built-in stress decreases from 460 to 410 MPa after irradiation.

To further study the radiation effects on the resonance of the fundamental mode, we irradiate the GaN/AlN doubly-clamped resonators on Chip 3, Chip 4, and Chip 5 with the fluence $\Phi = 10^{13}, 10^{14},$ and 10^{15} cm^{-2} , respectively. Fig. 7(a)–(d) shows the fundamental mode resonance spectra of the 300- and 400- μm long devices before and after radiation to fluence of 10^{14} cm^{-2} . Take the 300- μm long device as an example, the fundamental mode resonance frequency decreases from 499 to 124 kHz after irradiation. Similar trends are observed from the devices with different lengths. Compared with the results shown in Fig. 4, the fractional frequency downshifts much more dramatically for the devices irradiated with higher fluences, specifically, $\sim 20\%$ downshift for a fluence of 10^{13} cm^{-2} , $\sim 70\%$ downshift for a fluence of 10^{14} cm^{-2} , and $\sim 80\%$ downshift for a fluence of 10^{15} cm^{-2} . An earlier study suggests that the GaN crystal can become amorphous after high fluence ion irradiation [28]. Therefore, if we use the same analytical model and apply the Young's modulus of amorphous GaN, $E_{Y,\text{GaN}} = 65 \text{ GPa}$, into (1), we obtain the fundamental mode resonance frequency scaling

as a function of built-in stress [Fig. 7(e)]. By putting the experimentally measured resonances into the analytical model, we extract the built-in stress of the devices after irradiation. For fluences $\Phi \geq 10^{14} \text{ cm}^{-2}$, the postradiation built-in stress decreases significantly from 440 MPa to ~ 10 –70 MPa. For a fluence of 10^{13} cm^{-2} , a comparably moderate built-in stress change from 440 to ~ 330 MPa is induced in the 200- μm long devices. The results suggest that at high fluences ($\Phi \geq 10^{14} \text{ cm}^{-2}$), the mechanical properties of these GaN/AlN MEMS resonators can be severely altered by displacement damage. Fig. 8 summarizes the effects of fluence on the fractional downshift of the resonance frequency. For fluences less than 10^{13} cm^{-2} , the fractional downshift of resonance frequency is exponentially related to the fluence, namely increasing from 1% to 20% as the fluence changing from $\Phi = 5 \times 10^{11}$ to 10^{13} cm^{-2} . For fluences larger than 10^{14} cm^{-2} , the fractional frequency shift saturates at 70%–80%. As will be discussed later, this can be ascribed to the strong deformation of GaN/AlN doubly-clamped devices under extremely high radiation fluence ($\Phi \geq 10^{14} \text{ cm}^{-2}$). To the best of our knowledge, such large fractional shift of resonance frequency under radiation has not been reported in any other MEMS devices. The current body of research indicates that radiation response of MEMS devices is related to a broad range of factors, including materials, geometry, physical principles for sensing and actuation, and radiation sources with different ion species, energy, and fluence. The study of radiation effects on MEMS devices is still very limited and largely focused on Si MEMS. Although the reported changes of the resonance frequencies of most Si MEMS resonators are within hundreds of parts-per-million upon exposure to protons [18], [19], [29], the radiation fluences and doses therein are much lower than those in this work. A larger frequency downshift of 2%–3% is observed in a surface micromachined polysilicon doubly-clamped resonators irradiated by 32-krad gamma ray [30]. As a WBG semiconductor material, SiC has attracted a lot of attention in harsh environment applications. Upon 10.25-MeV oxygen ion irradiation, frequency downshifts of $\sim 6.6\%$ –11.3% are observed in the multimode resonances of the SiC diaphragms [20]. The very little frequency recovery indicates that the radiation effects on the mechanical properties of SiC are permanent and mainly associated with atom displacement [20]. Exploring the underlying physics of the effects of radiation on the material properties and device operations is essential along the way to employ MEMS devices in radiation environments. For our GaN/AlN MEMS resonators, the dramatic change of resonance frequency originates from the very high fluence and dose levels that we employ, which is useful for understanding potential degradation mechanisms and ensuring that there are no unexpected results at lower damage levels.

B. Radiation Effects on the Resonance of In-Plane Mode

Based on the rectangular cross-sectional shape and orientation of the GaN/AlN doubly-clamped structure, the flexural rigidity in the in-plane direction ($E_Y I_z = E_Y t w^3 / 12$) is more than fifty times larger than that in the out-of-plane direction ($E_Y I_y = E_Y w t^3 / 12$). Thus, the resonance frequencies

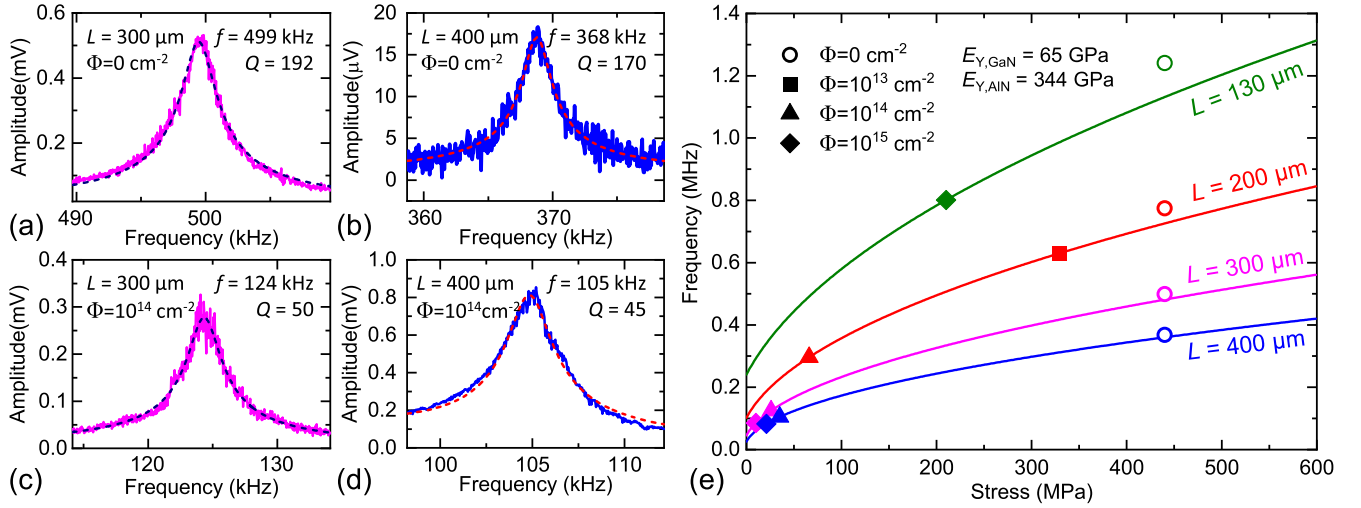


Fig. 7. Effects of ion irradiation on resonance frequencies of the GaN/AIN MEMS resonators. (a) and (b) Fundamental mode resonance spectra of unirradiated 300- and 400- μm long devices, respectively. (c) and (d) Fundamental mode resonance spectra of the same devices after 10^{14} cm^{-2} of 440-keV Ar^+ radiation. (e) Comparison of measured and calculated fundamental mode resonance frequencies with varying stress for $E_{Y,\text{GaN}} = 65 \text{ GPa}$. Symbols represent the measured frequencies, while the lines represent the calculated frequencies. Symbol shapes encode the fluences, while their colors correspond to various device lengths.

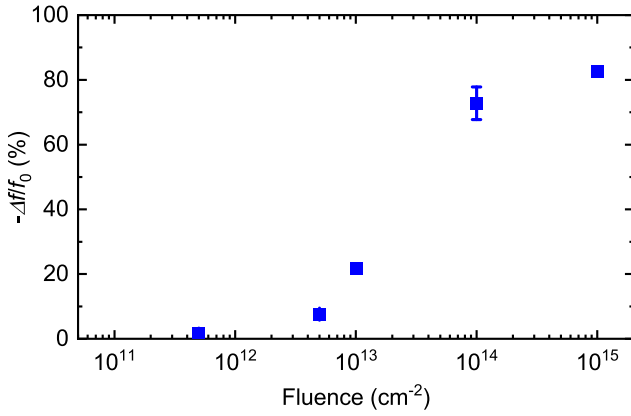


Fig. 8. Fractional downshift of fundamental out-of-plane mode resonance frequency with fluence of $\Phi = 5 \times 10^{11}$, 5×10^{12} , 10^{13} , 10^{14} , and 10^{15} cm^{-2} . There are three error bars for the data points with the fluence of 5×10^{11} , 5×10^{12} , and 10^{14} cm^{-2} . There is no error bar for the data points with the fluence of 10^{13} and 10^{15} cm^{-2} because only two devices are measurable with these two fluences.

of in-plane modes depend more on E_Y due to the large flexural rigidity. In other words, we can use the flexural rigidity dominant, “beam” model to describe the in-plane-mode resonance frequency. Thus, (1) can be simplified for the resonance frequency of the fundamental in-plane flexural ($L1$) mode

$$f_{L1} = \frac{9\pi}{8L^2} \sqrt{\frac{E_Y I_z}{\rho \omega t}} = \frac{3\sqrt{3}\pi w}{16L^2} \sqrt{\frac{E_Y}{\rho}}. \quad (3)$$

To study the radiation effects on the Young’s modulus, we measure and model the first in-plane flexural mode resonance of both unirradiated and radiated GaN/AIN doubly-clamped resonators. We first measure the resonance frequencies of the first in-plane mode of the unirradiated devices on Chip 1. The resonance frequencies are at 4.419, 1.398, 0.770, 0.520, 0.392, and 0.314 MHz, for $L = 100, 200, 300, 400, 500,$

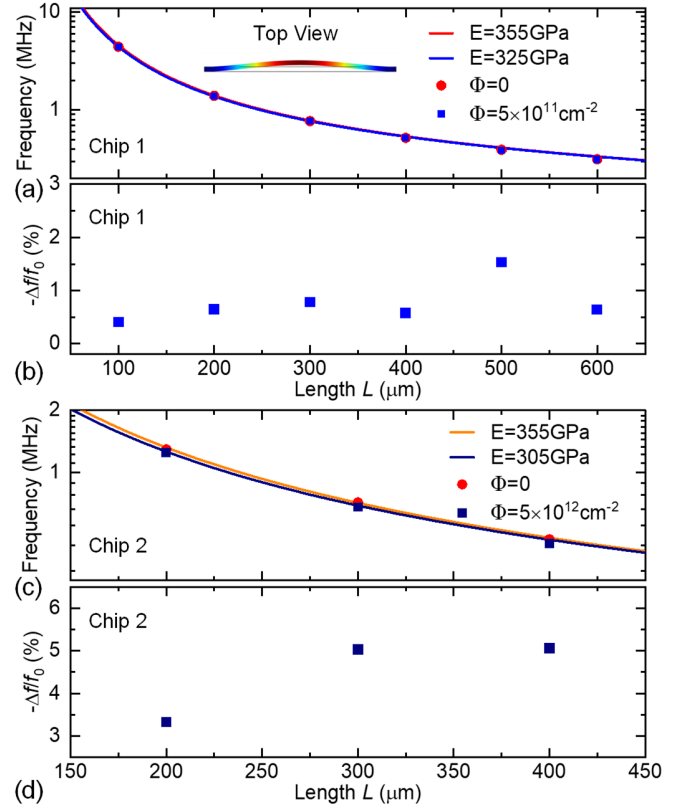


Fig. 9. (a) Resonance frequencies of the first in-plane flexural mode for devices with $L = 100, 130, 200, 300, 400, 500,$ and $600 \mu\text{m}$ before and after radiation with $\Phi = 5 \times 10^{11} \text{ cm}^{-2}$. Resonance frequency fitting with elastic beam resonator model from (a). (c) Resonance frequencies of the first in-plane mode for devices with $L = 200, 300,$ and $400 \mu\text{m}$ before and after radiation with $\Phi = 5 \times 10^{12} \text{ cm}^{-2}$. (d) Fractional downshift of resonance frequency from (c).

and $600 \mu\text{m}$ [Fig. 9(a)], respectively. The measured resonance frequencies before irradiation agree well with the analytical model [see (3)] by using $E_{Y,\text{GaN}} = 360 \text{ GPa}$, $E_{Y,\text{AlN}} = 344 \text{ GPa}$, $\rho_{\text{GaN}} = 6150 \text{ kg/m}^3$, and $\rho_{\text{AlN}} = 3260 \text{ kg/m}^3$.

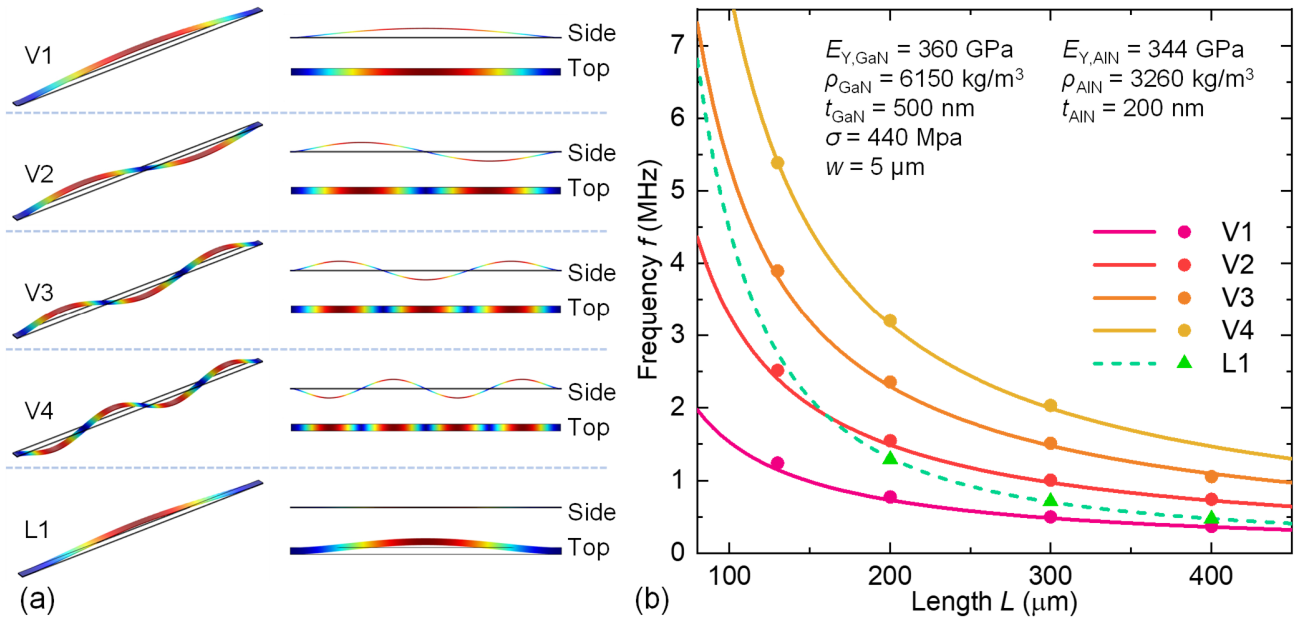


Fig. 10. (a) Mode shapes of four out-of-plane flexural modes (V1–V4) and one in-plane flexural mode (L1) of GaN/AlN doubly-clamped resonators. (b) Frequency scaling and measured multimode resonance frequencies of unirradiated resonators with different lengths. Symbols represent the measured frequencies, while the lines represent the calculated frequencies by (2) and (3).

After radiation with fluence of $5 \times 10^{11} \text{ cm}^{-2}$, the resonance frequencies shift slightly down. The fractional downshift of resonance frequencies of the first in-plane mode lies in the range of 0.5%–1.5% [Fig. 9(b)]. The measured frequencies of the first in-plane mode after irradiation agree well with the analytical model [see (3)] by using $E_Y = 325 \text{ GPa}$. Note here $E_Y = (E_{Y,\text{GaN}}t_{\text{GaN}} + E_{Y,\text{AlN}}t_{\text{AlN}})/(t_{\text{GaN}} + t_{\text{AlN}})$. Note that the effect of variation of built-in stress is negligible and does not impact the in-plane mode in the beam regime [see (3)]. Thus, a 30-GPa decrease of effective Young's modulus of the composite is induced after radiation at a fluence of $5 \times 10^{11} \text{ cm}^{-2}$.

We then measure the first in-plane mode resonance of the GaN/AlN doubly-clamped resonators on Chip 2, with $L = 200, 300, \text{ and } 400 \mu\text{m}$, before and after irradiation to a fluence of $5 \times 10^{12} \text{ cm}^{-2}$. Similar to what has been observed in out-of-plane fundamental mode V1 (Fig. 6), irradiation to a fluence of $5 \times 10^{12} \text{ cm}^{-2}$ induces a large decrease in the resonance frequency of the first in-plane mode, with the fractional downshift of the resonance frequency in the range of 3%–5% [Fig. 9(c) and (d)]. According to the analytical model [see (3)], this corresponds to a 50-GPa decrease in the effective composite Young's modulus.

C. Radiation Effects on Multimode Resonances

The equation for the multimode resonance frequency of the GaN/AlN doubly-clamped resonator is [27]

$$f_n = \frac{\pi(n+1/2)^2}{2L^2} \sqrt{\frac{E_Y I}{\rho w t}} \sqrt{1 + \frac{0.97\sigma w t L^2}{(n+1)^2 \pi^2 E_Y I}} \quad (4)$$

where n is the mode number. We measure and model the multimode resonances of unirradiated GaN/AlN doubly-clamped resonators on yet another chip (Chip 3) with different lengths,

as shown in Fig. 10. By using $E_{Y,\text{GaN}} = 360 \text{ GPa}$, $E_{Y,\text{AlN}} = 344 \text{ GPa}$, $\rho_{\text{GaN}} = 6150 \text{ kg/m}^3$, $\rho_{\text{AlN}} = 3260 \text{ kg/m}^3$, and $\sigma = 440 \text{ MPa}$, the analytical model agrees very well with the measured results [Fig. 10(b)]. For the 200- μm long device, five resonant modes are obtained from measurement. By matching the resonance frequencies to finite element method (FEM) simulation results, we confirm that four of them are out-of-plane flexural modes (V1–V4) and the other one is an in-plane flexural mode (L1), with the corresponding mode shapes shown in Fig. 10(a). The resonance frequencies of the out-of-plane modes show a clear stress-dominant behavior [see (2)], with the frequency ratio equal to the ratio of mode numbers, *i.e.*, $f_{Vn} : f_{V1} = n : 1$.

To better understand the effect of radiation on resonant behavior, we further measure the resonance frequencies of higher modes of the devices with length $L = 200, 300, \text{ and } 400 \mu\text{m}$ on Chip 3, Chip 4, and Chip 5 after irradiation with different fluences (Fig. 11). Similar to the method used in Fig. 6, we extract the built-in stress of the devices after irradiation using the analytical model. For a fluence of 10^{13} cm^{-2} , the built-in stress decreases from 440 MPa to the range of 230–400 MPa. At a higher fluence of 10^{14} cm^{-2} , the stress further decreases and lies within the range of 25–230 MPa. For the highest attempted fluence of 10^{15} cm^{-2} , the built-in stress decreases to below 25 MPa. The downshift of resonance frequency of the higher modes can be attributed to the displacement damage caused by Ar^+ irradiation, which significantly alters the mechanical properties.

D. Displacement Damage of the Doubly-Clamped Structures

Furthermore, the GaN/AlN doubly-clamped resonators are examined with high-resolution SEM imaging. While the unirradiated devices appear to be straight [Fig. 12(a) and (c)],

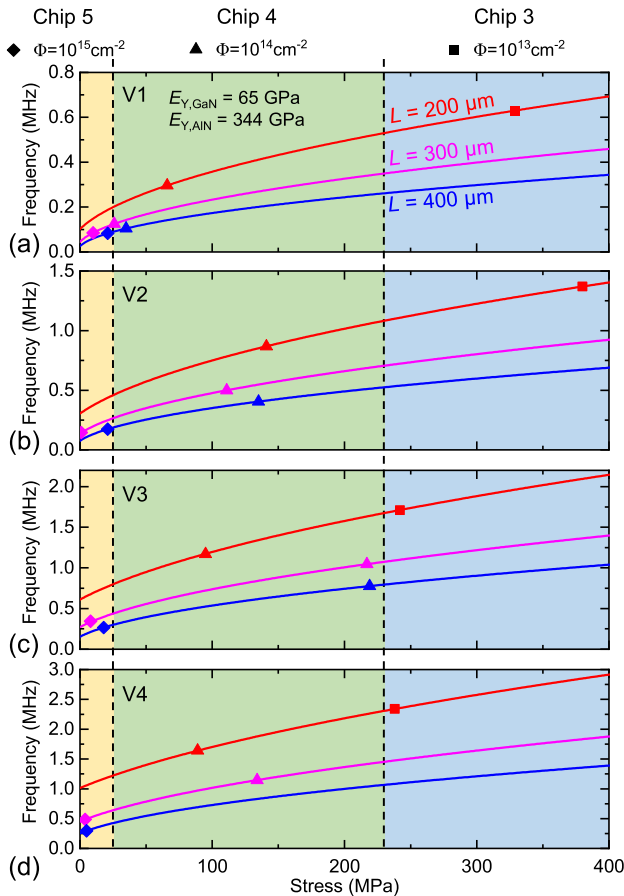


Fig. 11. Effects of ion irradiation on resonance frequencies of the GaN/AlN MEMS resonators with $L = 200, 300,$ and $400 \mu\text{m}$ for (a) first out-of-plane mode (V1), (b) second out-of-plane mode (V2), (c) third out-of-plane mode (V3), and (d) fourth out-of-plane mode (V4). Comparison of measured and calculated resonance frequencies of out-of-plane modes (V1–V4) at varying stress with $E_{Y,\text{GaN}} = 65 \text{ GPa}$.

the irradiated devices are severely deflected in the direction normal to the substrate [Fig. 12(b) and (d)], where the amount of deflection increases monotonically with the fluence [Fig. 12(e) and (f)]. The results suggest that the irradiation causes mechanical deformation of the suspended structures. The origin of the displacement damage can be ascribed to cumulative nonionizing radiation damage in the GaN layer. Unintentionally doped GaN is usually n-type due to the presence of common donor impurities, such as Si and O, which can be incorporated on Ga sites and N sites, respectively. The main defects in undoped GaN are predicted theoretically to be N and Ga vacancies, Ga interstitials, and anti-sites [31]–[33]. The concentration of these defects increases due to the additional defects introduced by the irradiation. At higher doses, the situation becomes more complicated, in which these defects may interact or form combinations with impurities to form more complex defects [14]. At high doses, extended crystalline defects and even amorphous layers will be generated. According to SRIM simulations (Fig. 1), the displacement damage is confined in the GaN layer, while the AlN layer is largely intact. Initial stress equilibrium is destroyed in the process and a new stress equilibrium state

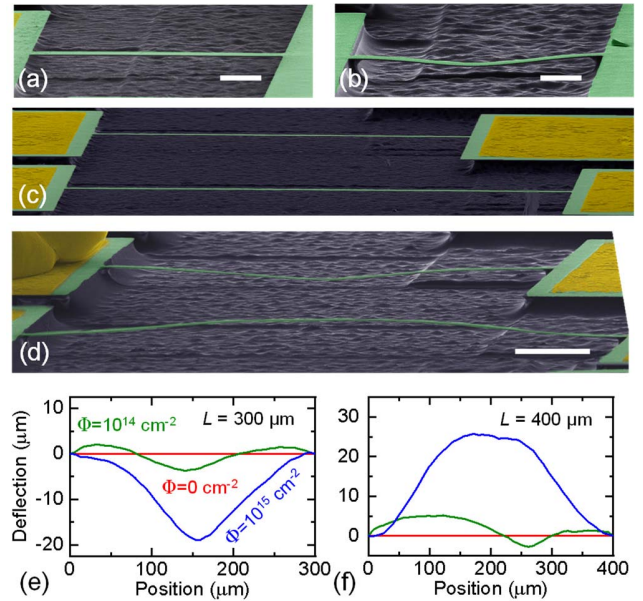


Fig. 12. Postirradiation deformation of GaN/AlN doubly-clamped resonators. Colored SEM image of $130\text{-}\mu\text{m}$ long resonator (a) without and (b) with $10^{15} \text{ cm}^{-2} \text{ Ar}^+$ irradiation. Scale bars: $20 \mu\text{m}$. Colored SEM image of 300- and $400\text{-}\mu\text{m}$ long resonators (c) without and (d) with $10^{15} \text{ cm}^{-2} \text{ Ar}^+$ irradiation. Scale bar: $50 \mu\text{m}$. (e) and (f) Profiles of the devices after different fluences of irradiation, in which the displacement is observed in the direction normal to the substrate.

evolves after irradiation. The displacement damage significantly alters Young's modulus and the built-in stress of the GaN/AlN resonators and causes deformation of the structures, which changes the resonance frequency. The results extend the understanding of radiation-induced damage mechanisms in GaN MEMS devices.

IV. CONCLUSION

In summary, we have investigated the effects of Ar^+ ion-induced displacement damage on doubly-clamped GaN/AlN MEMS resonators irradiated with extremely high level of doses. The multimode resonance frequencies of the devices decrease significantly with increasing fluence. The fractional downshift of resonance frequencies of out-of-plane fundamental mode V1 lies within the range of 1%–2.5% at the fluence of $5 \times 10^{11} \text{ cm}^{-2}$. The fractional downshift increases with the fluence, specifically, $\sim 8\%$ downshift for $\Phi = 5 \times 10^{12} \text{ cm}^{-2}$, $\sim 20\%$ downshift for $\Phi = 10^{13} \text{ cm}^{-2}$, $\sim 70\%$ downshift for $\Phi = 10^{14} \text{ cm}^{-2}$, and $\sim 80\%$ downshift for $\Phi = 10^{15} \text{ cm}^{-2}$. SEM imaging shows that the highly irradiated GaN/AlN resonators are severely deflected, where the amount of deflection varies monotonically with the fluence. The results suggest that the displacement damage significantly alters Young's modulus and the built-in stress of the GaN/AlN resonators and causes deformation of the structures. Although relatively much smaller changes in the MEMS resonators' parameters would be expected in typical space environments, our results provide useful information for understanding radiation-induced damage mechanisms in GaN MEMS devices, and may be useful in applications such as nuclear reactors or particle accelerators where very high radiation levels are encountered.

REFERENCES

- [1] O. Solgaard, A. A. Godil, R. T. Howe, L. P. Lee, Y.-A. Peter, and H. Zappe, "Optical MEMS: From micromirrors to complex systems," *J. Microelectromech. Syst.*, vol. 23, no. 3, pp. 517–538, Jun. 2014.
- [2] R. Nathanael, V. Pott, H. Kam, J. Jeon, and T.-J. K. Liu, "4-terminal relay technology for complementary logic," in *IEDM Tech. Dig.*, Baltimore, MD, USA, Dec. 2009, pp. 223–226.
- [3] X. L. Feng, M. H. Matheny, C. A. Zorman, M. Mehregany, and M. L. Roukes, "Low voltage nanoelectromechanical switches based on silicon carbide nanowires," *Nano Lett.*, vol. 10, no. 8, pp. 2891–2896, Aug. 2010.
- [4] A. Yao and T. Hikihara, "Logic-memory device of a mechanical resonator," *Appl. Phys. Lett.*, vol. 105, no. 12, Sep. 2014, Art. no. 123104.
- [5] J. Yaug, L. Hutin, J. Jeon, and T.-J.-K. Liu, "Adhesive force characterization for MEM logic relays with sub-micron contacting regions," *J. Microelectromech. Syst.*, vol. 23, no. 1, pp. 198–203, Feb. 2014.
- [6] G. Kotzar *et al.*, "Evaluation of MEMS materials of construction for implantable medical devices," *Biomaterials*, vol. 23, pp. 2737–2750, Jul. 2002.
- [7] A. Chaalane *et al.*, "A MEMS-based solid propellant microthruster array for space and military applications," *J. Phys., Conf. Ser.*, vol. 660, no. 1, 2015, Art. no. 012137.
- [8] T. G. Brown, "Harsh military environments and microelectromechanical (MEMS) devices," in *Proc. SENSORS*, vol. 2, Oct. 2003, pp. 753–760.
- [9] W. M. Van Spengen, "MEMS reliability from a failure mechanisms perspective," *Microelectron. Rel.*, vol. 43, no. 7, pp. 1049–1060, Jul. 2003.
- [10] Y. Huang, A. S. S. Vasan, R. Doraiswami, M. Osterman, and M. Pecht, "MEMS reliability review," *IEEE Trans. Device Mater. Rel.*, vol. 12, no. 2, pp. 482–493, May 2012.
- [11] C. N. Arutt *et al.*, "The study of radiation effects in emerging micro and nano electro mechanical systems (M and NEMs)," *Semicond. Sci. Technol.*, vol. 32, no. 1, Jan. 2017, Art. no. 013005.
- [12] P. Gkotsis *et al.*, "Neutron and gamma radiation effects on MEMS structures," *Proc. Eng.*, vol. 25, pp. 172–175, Jan. 2011.
- [13] S. Garcia-Blanco, H. R. Shea, and R. Ramesham, "Effects of radiation on MEMS," *Proc. SPIE Rel., Packag., Test., Characterization MEMS/MOEMS Nanodevices*, vol. 7928, Feb. 2011, Art. no. 79280E.
- [14] S. J. Pearton, F. Ren, E. Patrick, M. E. Law, and A. Y. Polyakov, "Review—Ionizing radiation damage effects on GaN devices," *ECS J. Solid State Sci. Technol.*, vol. 5, no. 2, pp. Q35–Q60, Nov. 2015.
- [15] J. R. Srouf, C. J. Marshall, and P. W. Marshall, "Review of displacement damage effects in silicon devices," *IEEE Trans. Nucl. Sci.*, vol. 50, no. 3, pp. 653–670, Jun. 2003.
- [16] J. Lee, M. J. Krupcale, and P. X.-L. Feng, "Effects of γ -ray radiation on two-dimensional molybdenum disulfide (MoS_2) nanomechanical resonators," *Appl. Phys. Lett.*, vol. 108, no. 2, Jan. 2016, Art. no. 023106.
- [17] M. Rais-Zadeh, V. J. Gokhale, A. Ansari, M. Faucher, D. Théron, Y. Cordier, and L. Buchailot, "Gallium nitride as an electromechanical material," *J. Microelectromech. Syst.*, vol. 23, no. 6, pp. 1252–1271, Dec. 2014.
- [18] J. Gomes and H. R. Shea, "Displacement damage effects in silicon MEMS at high proton doses," *Proc. SPIE Rel., Packag., Test., Characterization MEMS/MOEMS Nanodevices*, vol. 7928, Feb. 2011, Art. no. 79280G.
- [19] H. Gong *et al.*, "Proton-induced displacement damage and total-ionizing-dose effects on silicon-based MEMS resonators," *IEEE Trans. Nucl. Sci.*, vol. 65, no. 1, pp. 34–38, Jan. 2018.
- [20] H. Chen *et al.*, "Probing heavy ion radiation effects in silicon carbide (SiC) via 3D integrated multimode vibrating diaphragms," *Appl. Phys. Lett.*, vol. 114, no. 10, Mar. 2019, Art. no. 101901.
- [21] H. Chen, H. Jia, P. D. Shuvra, J.-T. Lin, B. W. Alphenaar, and P. X.-L. Feng, "GaN/AlN heterostructure micromechanical self-sustained oscillator for middle ultraviolet (MUV) light detection," in *Proc. IEEE 32th Int. Conf. Micro Electro Mech. Syst. (MEMS)*, Jan. 2019, pp. 644–647.
- [22] J. Lin *et al.*, "Impact of X-ray radiation on GaN/AlN MEMS structure and GaN HEMT gauge factor response," in *Proc. 33rd IEEE Int. Conf. Micro Electro Mech. Syst. (MEMS)*, Vancouver, BC, Canada, Jan. 2020, pp. 968–971.
- [23] S. R. Messenger *et al.*, "Nonionizing energy loss (NIEL) for heavy ions," *IEEE Trans. Nucl. Sci.*, vol. 46, no. 6, pp. 1595–1602, Dec. 1999.
- [24] R. Kirste *et al.*, "Compensation effects in GaN: Mg probed by Raman spectroscopy and photoluminescence measurements," *J. Appl. Phys.*, vol. 113, no. 10, Mar. 2013, Art. no. 103504.
- [25] W. Sui, X.-Q. Zheng, J.-T. Lin, B. W. Alphenaar, and P. X.-L. Feng, "Thermal response and TC f of GaN/AlN heterostructure multimode micro string resonators from -10°C up to 325°C ," *J. Microelectromech. Syst.*, vol. 30, no. 4, pp. 521–529, Aug. 2021.
- [26] W. Sui, X.-Q. Zheng, J.-T. Lin, B. W. Alphenaar, and P. X.-L. Feng, "Temperature dependence of multimode gallium nitride/aluminum nitride (GaN/AlN) heterostructure string resonator," in *Proc. IEEE 34th Int. Conf. Micro Electro Mech. Syst. (MEMS)*, Jan. 2021, pp. 478–481.
- [27] A. Bokaian, "Natural frequencies of beams under tensile axial loads," *J. Sound Vib.*, vol. 142, no. 3, pp. 481–498, Nov. 1990.
- [28] S. O. Kucheyev, J. E. Bradby, J. S. Williams, C. Jagadish, M. V. Swain, and G. Li, "Deformation behavior of ion-beam-modified GaN," *Appl. Phys. Lett.*, vol. 78, no. 2, pp. 156–158, Jan. 2001.
- [29] T. Bandi, J. Baborowski, A. Dommann, H. R. Shea, F. Cardot, and A. Neels, "Evaluation of silicon tuning fork resonators under mechanical loads and space-relevant radiation conditions," *J. Micro/Nanolithography*, vol. 13, no. 4, Dec. 2014, Art. no. 043019.
- [30] L. Wang, J. Tang, and Q.-A. Huang, "Gamma irradiation effects on surface-micromachined polysilicon resonators," *J. Microelectromech. Syst.*, vol. 20, no. 5, pp. 1071–1073, Oct. 2011.
- [31] C. G. Van de Walle and J. Neugebauer, "First-principles calculations for defects and impurities: Applications to III-nitrides," *J. Appl. Phys.*, vol. 95, no. 8, pp. 3851–3879, 2004.
- [32] M. A. Reshchikov and H. Morko, "Luminescence properties of defects in GaN," *J. Appl. Phys.*, vol. 97, no. 6, pp. 5–19, Mar. 2005.
- [33] K. H. Chow, G. D. Watkins, A. Usui, and M. Mizuta, "Detection of interstitial Ga in GaN," *Phys. Rev. Lett.*, vol. 85, no. 13, pp. 2761–2764, Sep. 2000.